Supporting Information

Ni-Fe Synergic Effect in Fe-NiOH$_x$ Boosting Oxygen Evolution under Large Current Density Enabled by the "In-Situ Self-Corrosion" Strategy

Liang-ai Huang, [†, a] Jiu Chen, [†, b] Yue Xu, [a] Yucong Huang, [a] Shijie Shen, [a] Zongpeng Wang, [a] Lei Li, [*, b] and Wenwu Zhong, [*, a]

a School of Materials Science and Engineering, Taizhou University, No. 1139, Shifu Road, Taizhou 318000 (P. R. China)

b Department of Materials Science and Engineering, Southern University of Science and Technology, Shenzhen 518055 (P. R. China)

[†] These authors contributed equally to this work

*Corresponding author: Lei Li (lil33@sustech.edu.cn)

Wenwu Zhong (zhongww@tzc.edu.cn)

Experimental Section

Chemicals. Nickel sulfate hexahydrate (NiSO$_4$·6H$_2$O, AR), ammonium ferrous sulfate ((NH$_4$)$_2$Fe(SO$_4$)$_2$, AR), sodium acetate (NaAc, AR), zinc acetate dihydrate (Zn(AC)$_2$·2H$_2$O, AR), sodium hydroxide (NaOH, AR), Hexamethylenetetramine (HTMA, AR), zinc nitrate tetrahydrate (Zn(NO$_3$)$_2$·6H$_2$O, AR), concentrated nitric acid (HNO$_3$, AR), cobalt chloride hexahydrate (CoCl$_2$·6H$_2$O, AR), manganese dichloride (MnCl$_2$, AR), ammonium fluoride (NH$_4$F, AR), carbon cloth.

Synthesis of ZnO@NCC. All chemical reagents used were analytical grade without further purification. The carbon cloth was surface functioned using concentrated HNO$_3$ for 24 h at 90 °C to improve its hydrophilicity, then washed several times with deionized water and dried in vacuum at 60 °C. Further N-doping treatment of carbon cloth to increase its roughness and the electronic conductivity mainly involves three steps: hydrothermal reaction, thermal reduction, and concentrated acid treatment, as reported in the related literature.[1] ZnO@NCC was synthesized by the hydrothermal method, as described in our previous investigations.[2] In a detailed fabrication process, a piece of NCC (1.0 cm $\times$ 1.5 cm) was immersed in the seeding solution containing 0.01 M Zn(Ac)$_2$·2H$_2$O and 0.01 M NaOH, and then hydrothermal treatment at 150 °C for 15 min. The above seeding process was repeated four times. After that, the growth solution of 0.10 M hexamethylenetetramine (HMTA) and 0.10 M Zn(NO$_3$)$_2$·6H$_2$O was dissolved in deionized water separately, then mixed and stirred for 30 min. Then the NCC covered with the ZnO seed layer and the growth solution were transferred together to a 20 mL autoclave reactor and heated at a constant temperature of 100 °C for 12 h. Finally, the obtained film sample was rinsed thoroughly with deionized water and annealed under the Ar atmosphere at 400 °C for 1 h to obtain the ZnO@NCC substrate.

Synthesis of Fe-NiOH$_x$/ZnO@NCC. The Fe-NiOH$_x$/ZnO@NCC composite films were fabricated through a photochemical deposition method. Different molar

concentrations of $(NH_4)_2Fe(SO_4)_2$, 0.033 M $NiSO_4 \cdot 6H_2O$ and 0.033 M CH_3COONa formed the photochemical solution. The ZnO@NCC substrate (1.0 cm $\times$ 1.5 cm) and the Pt electrode were connected by a Cu wire and placed in the photodeposition reactor containing the mentioned photochemical solution. For the photodeposition of Fe-NiOH$_x$, the ZnO@NCC substrate was exposed to the UV–vis light irradiation (500 W Xe lamp, 2.0 mW cm^{-2}) through the quartz window, and the exposed area was ~1 cm^2. In the process of photodeposition, the solution was stirred constantly to ensure the uniformity of the deposition solution. The composite film was obtained after 3 h of photodeposition, then rinsed with deionized water several times and dried in a N_2 stream.

Synthesis of NiOH$_x$/ZnO@NCC and FeOH$_x$/ZnO@NCC. The fabrication process of NiOH$_x$/ZnO@NCC and FeOH$_x$/ZnO@NCC is the same as that of the Fe-NiOHx/ZnO@NCC sample, except that there are no $(NH_4)_2Fe(SO_4)_2$ and $NiSO_4 \cdot 6H_2O$ in the photodeposition solution, respectively.

Physical Characterizations. The structures of the fabricated film samples were characterized by X-ray diffraction (XRD) on the D/MAX 2550 X ray diffractometer from Rigaku company using Cu Kα radiation. Scanning electron microscopy (SEM, Carl Zeiss, Ultra 55) at an acceleration voltage of 5 kV and high-resolution transmission electron microscopy (TEM, Tecnai G2 F30) with an accelerating voltage of 200 kV were used to observe the morphologies and microstructures of the films. X-ray photoelectron spectroscopy (XPS) data were recorded using the Escalab 250Xi X-ray physical electronics photoelectron spectrometer with Mg Kα radiation. The obtained spectra were corrected according to the adventitious C *1s* peak (284.8 eV). Raman spectra were performed on a Raman spectrometer (Bruker Senterra II).

Electrochemical measurements. The electrochemical measurements were conducted on an electrochemical workstation (CHI 760E) based on the three-electrode system at room temperature. The as-prepared Fe-NiOH$_x$ composite film was used as

the working electrode, while Hg/HgO electrode (filled with 1 M KOH solution) and platinum foil were utilized as the reference electrode and the counter electrode, respectively. 1 M KOH aqueous solution was employed as an electrolyte. The electrocatalytic activity of the Fe-NiOH$_x$ composite film was measured by LSV at a scan rate of 5 mV s^{-1} with 95% *iR* drop compensation. The stability performance of the Fe-NiOH$_x$ composite film was tested using chronopotentiometry at a current density of 10 and 100 mA cm^{-2}. Electrochemical impedance spectroscopy (EIS) was conducted within the frequency range of 100 kHz to 0.1 Hz at the open circuit potential to obtain the solution impedance (*Rs*) of the electrochemical system and investigate the kinetics of the electrocatalysts. The electrochemical active surface area (ECSA) was determined on the basis of the measured double-layer capacitance (C$_{dl}$), which was calculated by CV curves within a potential range of 0.1 V centered at open-circuit potential at different scan rates.

Computational methods

All calculations were performed using the unrestricted density functional theory methods implemented in Vienna Ab initio Simulation Package (VASP).[3] The Perdew-Berke-Ernzerhof (PBE) functional plus Hubbard *U* correction was used to describe the exchange-correlation interaction.[4-5] The *U-J* values were set to 5.5 and 3.3 eV for Fe and Ni, respectively.[6-7] The energy cutoff and convergence criteria are 500 eV and 10^{-5} eV, respectively. All structures were relaxed until forces on each atom were less than 0.05eV/Å. A $4 \times 1 \times 1$ ($6 \times 2 \times 6$) k-point mesh centered at the Γ point was adopted for the slab (bulk) model.

A 4×1 supercell of the (102) surface cleaved from the jamborite Ni(OH)$_2$ bulk is used to model the Fe-doped and Fe-free nickel oxyhydroxide. Note that the simulated XRD of the jamborite Ni(OH)$_2$ with 20% H atoms removed matches with experimental data (Fig. S1). The surface Ni atoms are saturated with one layer of OH groups.[8] The as-build slab model consists of five trilayers of the *v*-shaped HO-Ni-OH with half of the atomic layers fixed (Fig. S2).

The hydrogen electrode model developed by Norskov and coworkers was used to compute free energies of the intermediates in the OER with the following equation.

$$\Delta G = \Delta E + \Delta ZPE - T\Delta S - eU$$

Where ΔE, ΔZPE, ΔS, e and U represent the difference of total energy calculated from DFT, zero-point energy, entropy, the number of transferred electrons and the applied potential, respectively. Overpotential is evaluated as the difference between the largest energy change of elementary steps during the OER pathway and the thermodynamic equilibrium potential (1.23 eV of water).

Supporting Figures and Tables
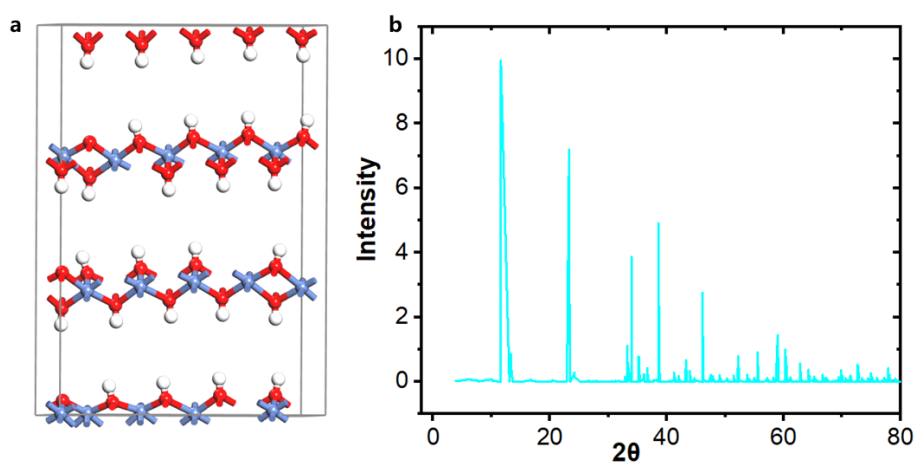
Fig. S1. (a) The atomic structure and (b) the corresponding computed XRD of the $Ni_5O(OH)_9$. The same color code as Fig. 4 is used.
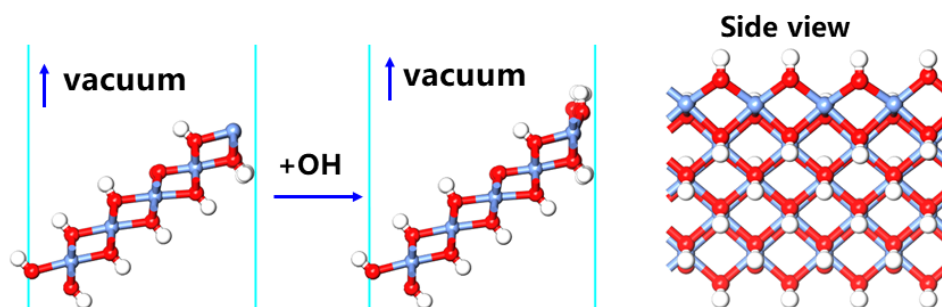
Fig. S2. The atomic structures of the Ni-terminated (left) and the OH-saturated (102) surface (middle). The right panel represents the side view of the OH-saturated (102) surface. The same color code as Fig. 4 is used.
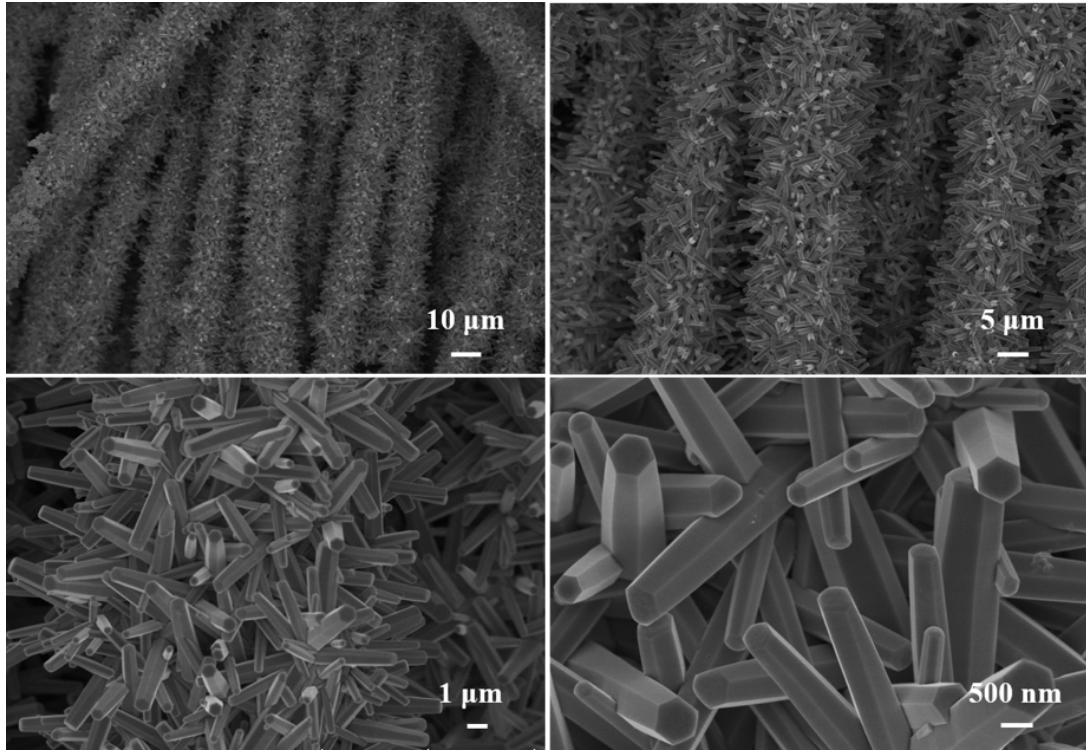
Fig. S3. SEM images of ZnO nanorods.
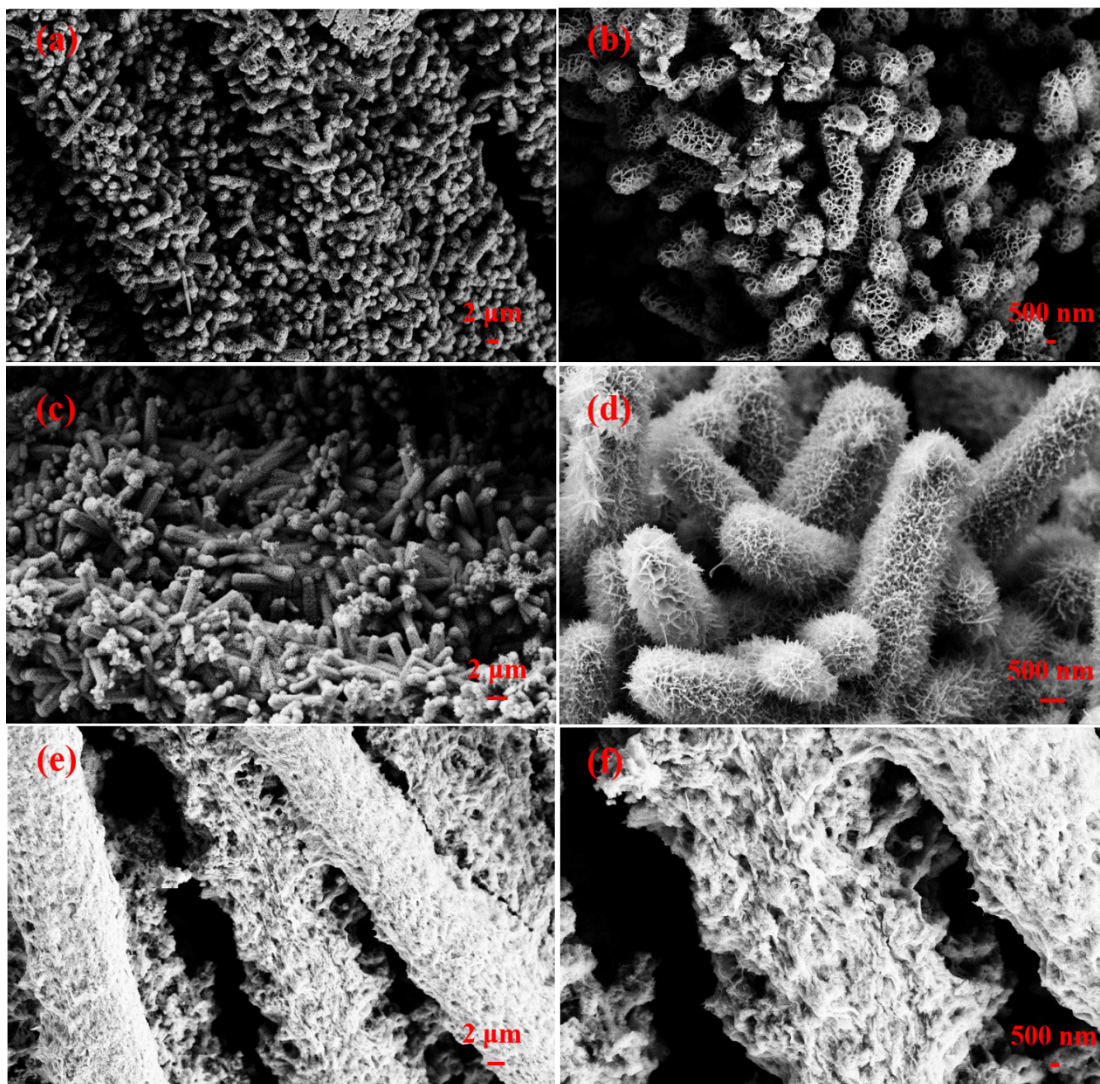
Fig. S4. SEM images of NiOH$_x$/ZnO (a-b), Fe-NiOH$_x$/ZnO (c-d) and FeOH$_x$/ZnO (e-f) catalysts.
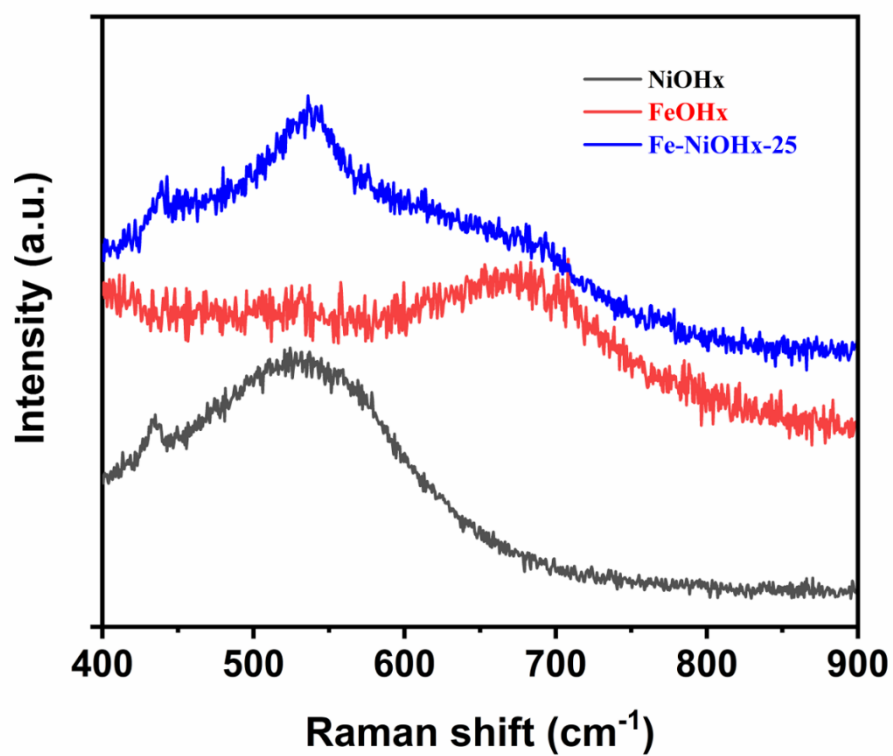
Fig. S5. Raman spectra of the as-fabricated NiOH$_x$/ZnO, Fe-NiOHx/ZnO,and FeOH$_x$/ZnO catalysts.
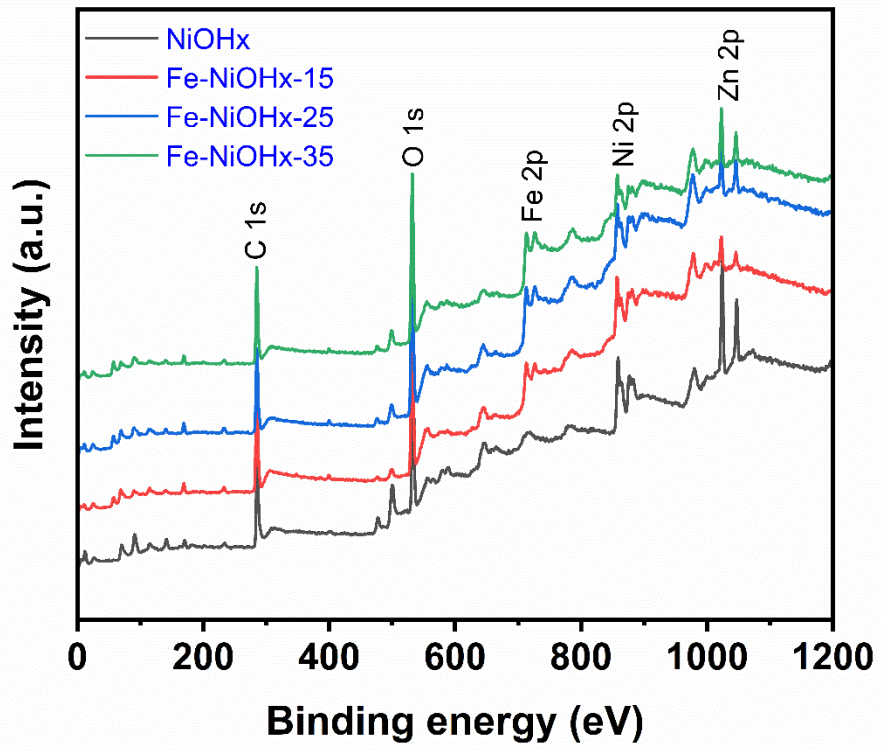
Fig. S6. Survey XPS patterns of the Fe-NiOH$_x$/ZnO and NiOH$_x$/ZnO film samples.
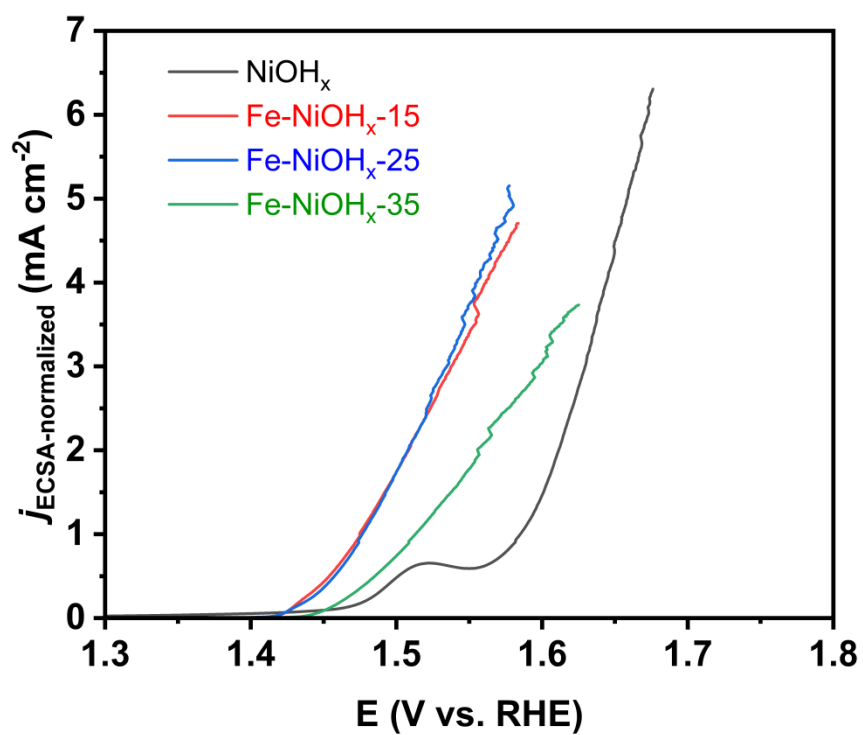
Figure S7. LSV curves of the as-fabricated $NiOH_x$ and $Fe-NiOH_x$ catalysts normalized by ECSA ($j_{ECSA-normalized}$).
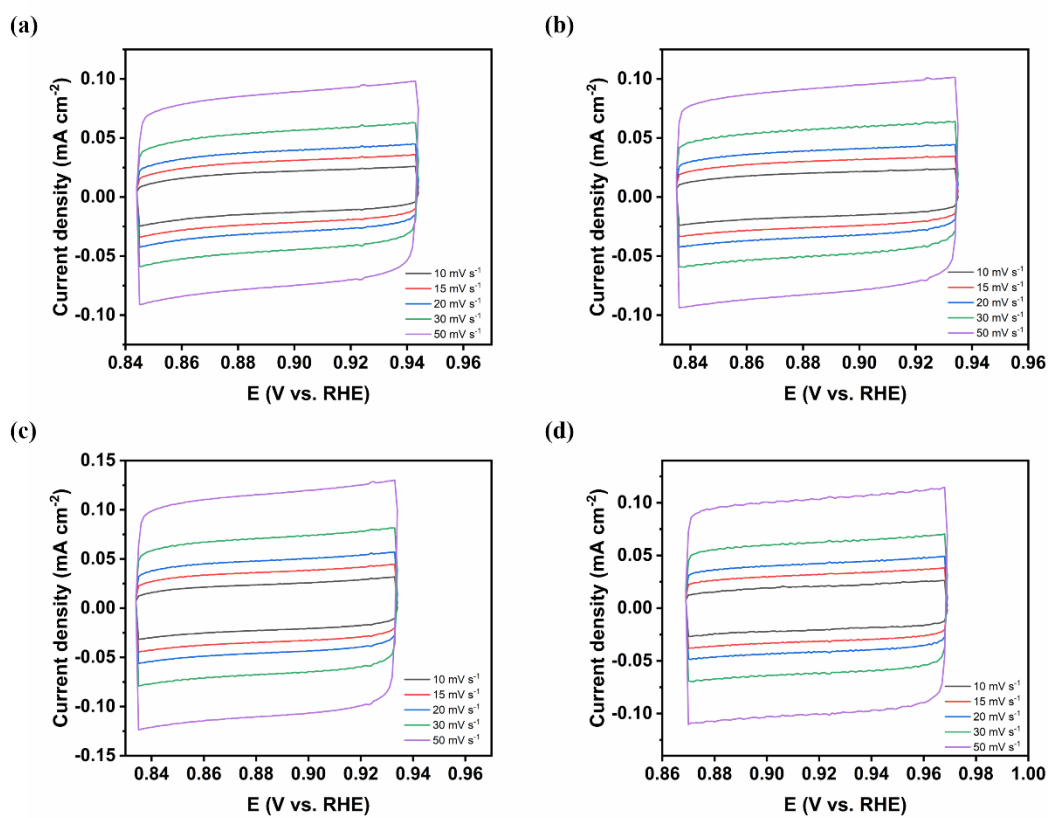
Fig. S8. C_{dl} of the NiOH$_x$/ZnO (a), Fe-NiOH$_x$-15 (b), Fe-NiOH$_x$-25 (c) and Fe-NiOH$_x$-35 (d) film samples.
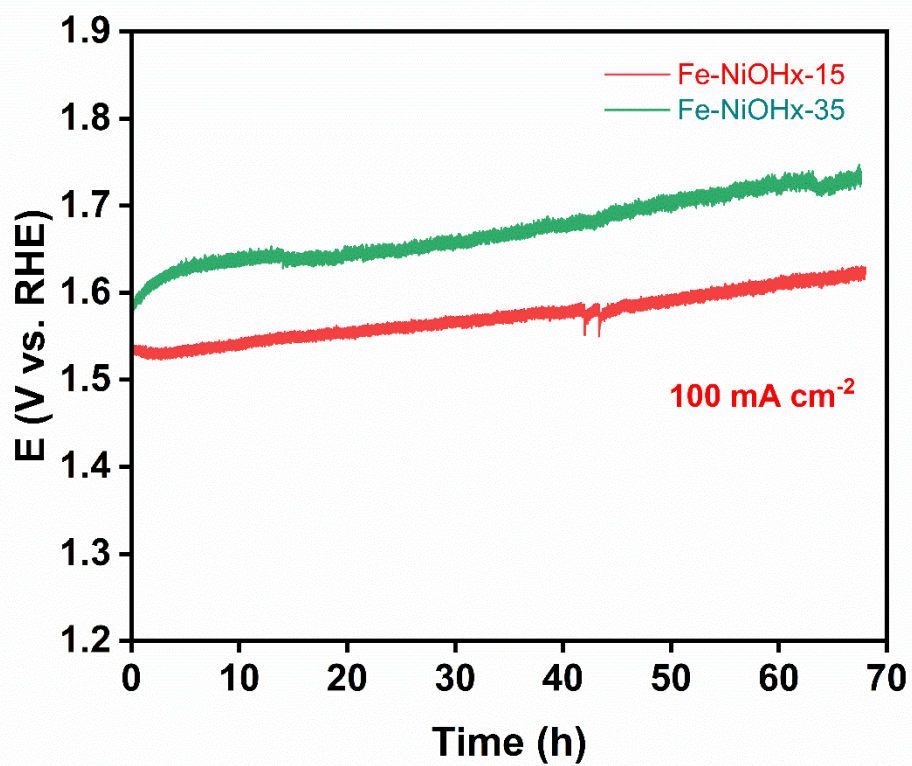
Fig. S9. Durability tests of the Fe-NiOH$_x$-15 and Fe-NiOH$_x$-35 electrodes at 100 mA cm^{-2}.
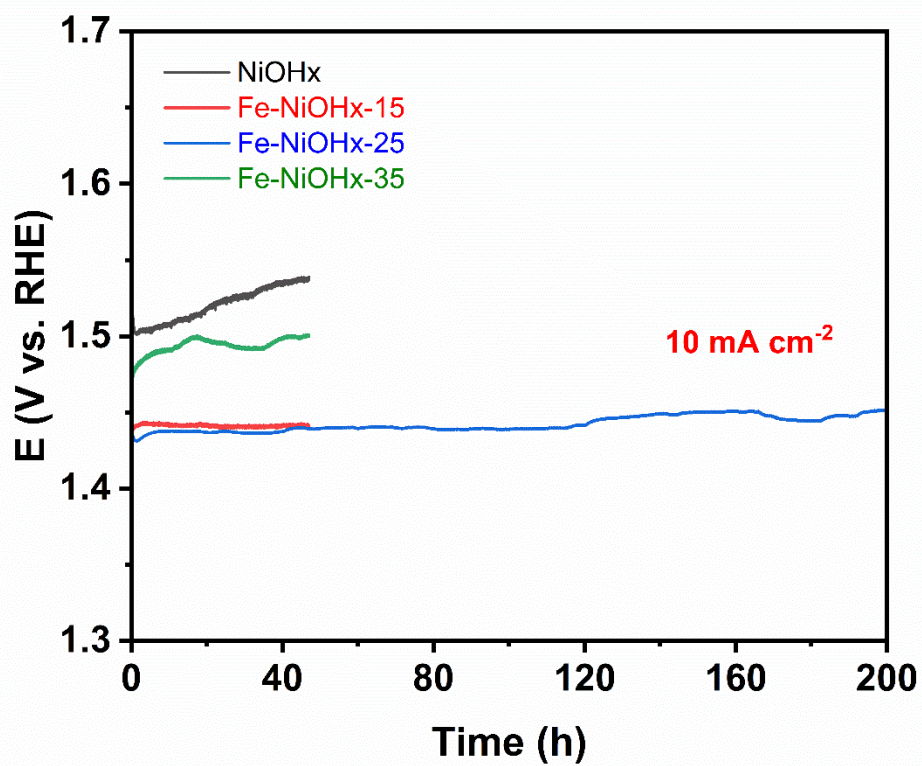
Fig. S10. Durability tests of the $NiOH_x$, $Fe-NiOH_x-15$, $Fe-NiOH_x-25$ and $Fe-NiOH_x-35$ electrodes at 10 mA cm^{-2}.
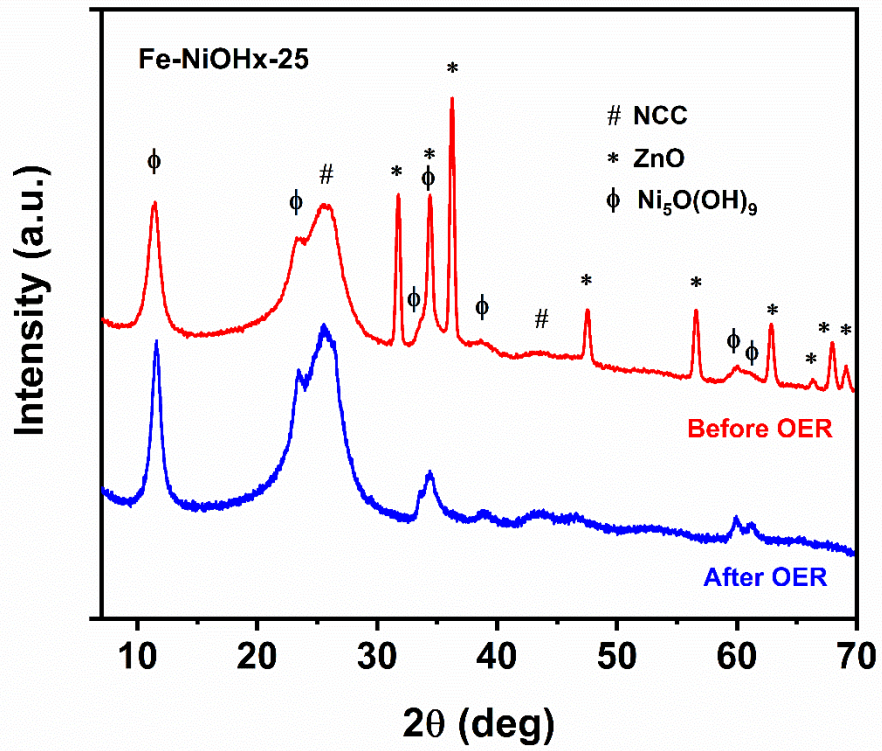
Fig. S11. XRD patterns of the Fe-NiOH$_x$-25 film samples before and after OER test.
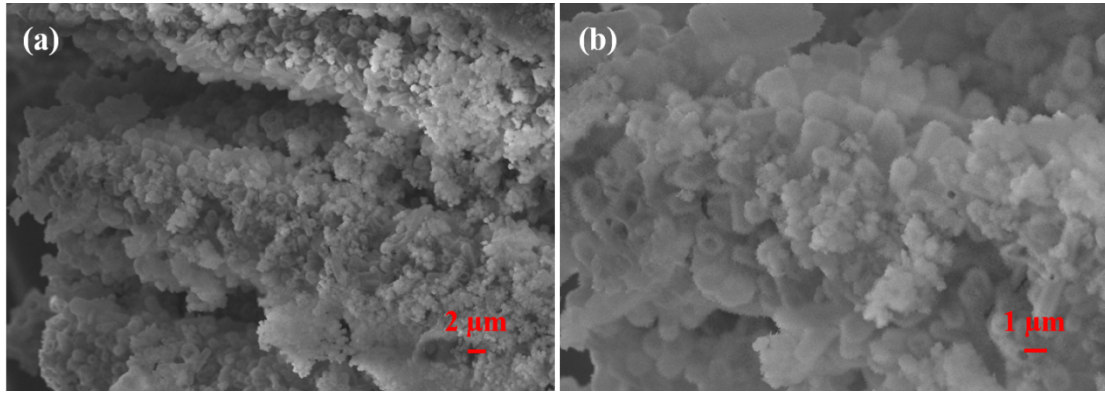
Figure S12. SEM images of Fe-NiOH$_x$-25 after a 240-h durability tests at a current density of 100 mA cm^{-2}.
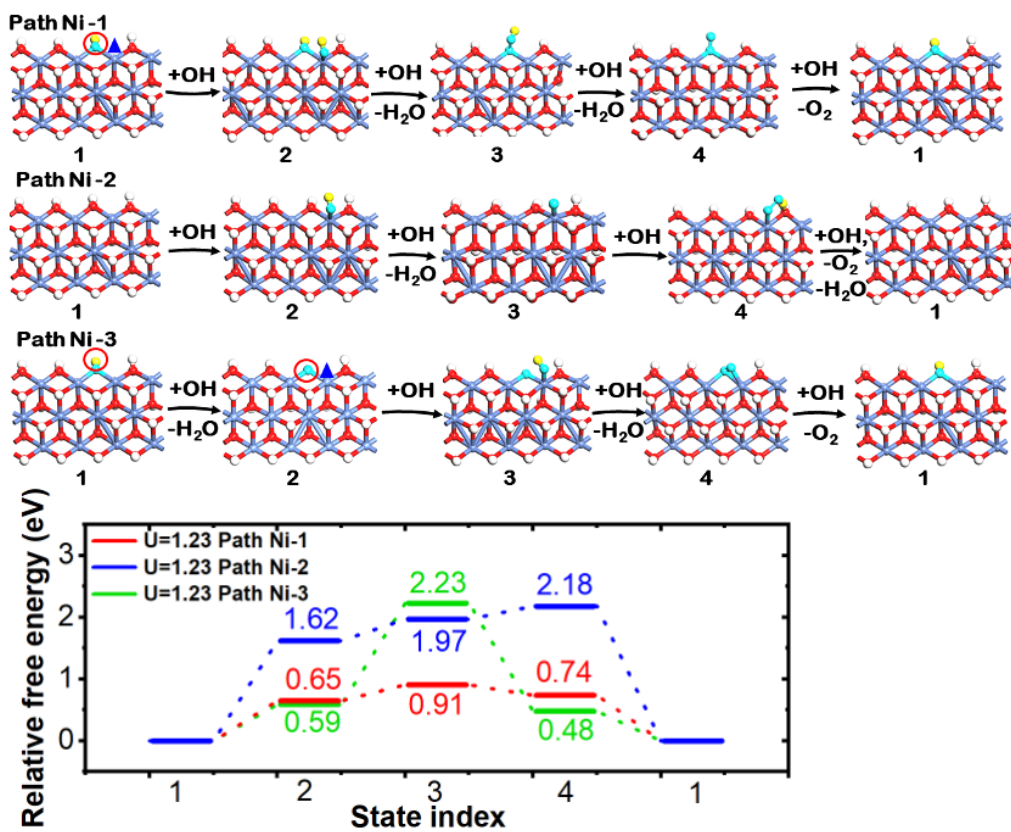
Fig. S13. Illustration of the reaction paths of the OER on the Fe-free $NiOH_x$. The corresponding free-energy profiles calculated at U=1.23 eV are shown in the bottom panel. The number below each structure corresponds to the state index in the bottom panel. The same color code as Fig. 4 is used.
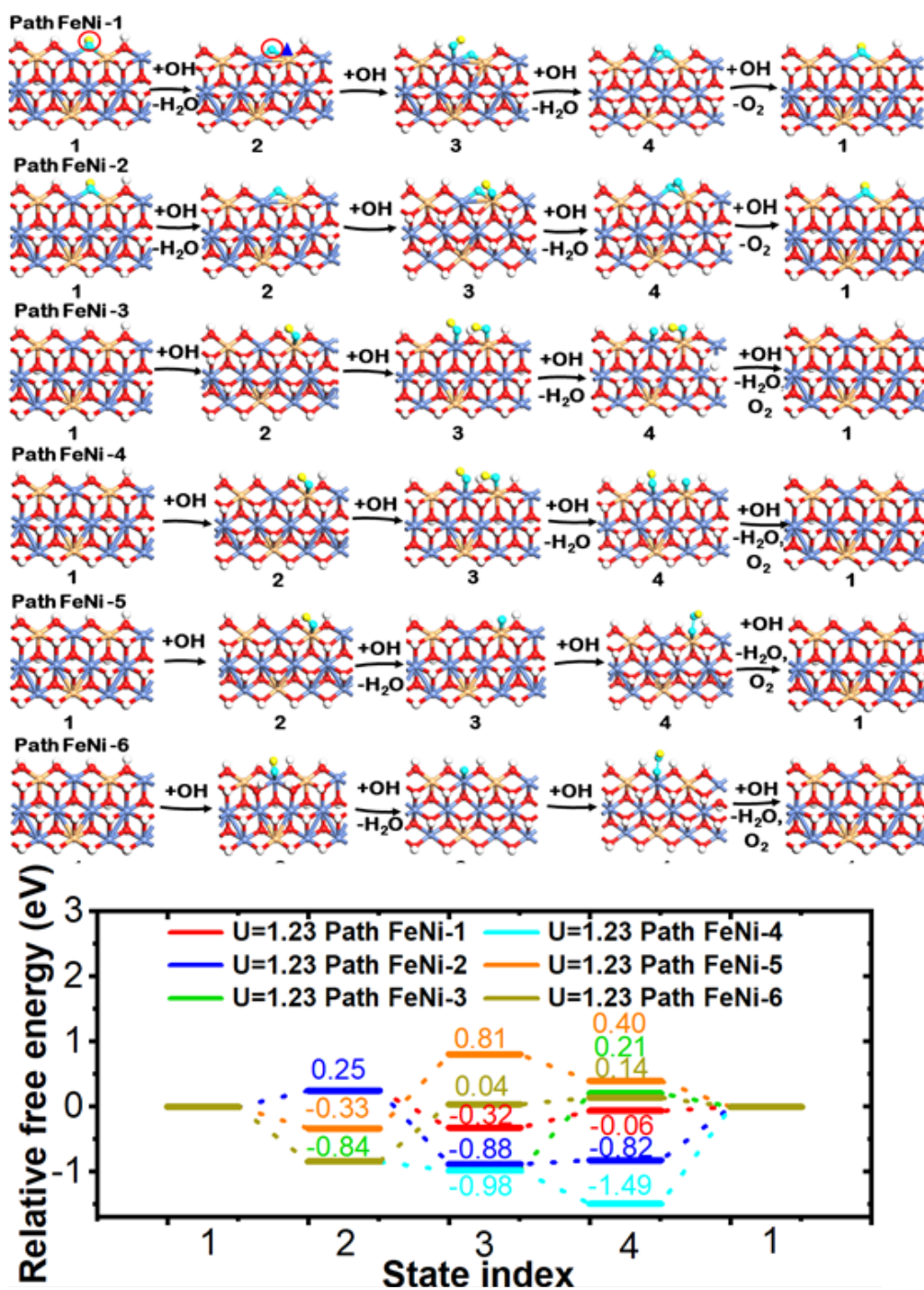
Fig. S14. Illustration of the reaction paths of the OER on the Fe-doped $NiOH_x$. The corresponding free-energy profiles calculated at U=1.23 eV are shown in the bottom panel. The number below each structure corresponds to the state index in the bottom panel. The same color code as Fig. 5 is used.

Table S1. Comparison of the electrocatalytic OER activity of recently reported NiFe-based electrocatalysts in basic electrolyte.

Catalysts	η_{10} (mV)	Durability (h)	Electrolyte	Ref.
NiFe LDH	290	6.9@ 10 mA/cm^{-2}	1.0 M KOH	9
NiFeO$_x$/Co-N$_y$-C	310	--	1.0 M KOH	10
O-NiCoFe LDH	340	10@ 100 mA/cm^{-2}	0.1 M KOH	11
NiCoFeO$_x$	410	--	0.1 M KOH	12
nNiFe LDH/NGF	337	3.3@ η=350 mV	0.1 M KOH	13
NiFeMo nanosheet	280	10@ 50 mA/cm^{-2}	1.0 M KOH	14
NiFe/NiCoO$_2$	286	--	1.0 M KOH	15
NiFe$_2$O$_4$	381	2@ η=470 mV	1.0 M KOH	16
NP Au/Cr-NiFe oxyhydroxide	323	55@ 10 mA/cm^{-2}	0.1 M KOH	17
NiO/NiFe$_2$O$_4$	302	2@ 20 mA/cm^{-2}	1.0 M KOH	18
(Co,Ni)Se$_2$@NiFe LDH	277	17@ 10 mA/cm^{-2}	1.0 M KOH	19
Ni-Fe LDH hollow nanoprisms/NF	280	6@ η=295 mV	1.0 M KOH	20
Fe Doped NiO	310	2@ 10 mA/cm^{-2}	0.5 M KOH	21
Fe Doped NiO	297	--	0.5 M KOH	22
Fe Doped NiOx with Ni^{3+} ions	310	18@ η=320 mV	1.0 M KOH	23
Fe Doped Mesoporous NiO	206	20@ η=235 mV	1.0 M KOH	24
Fe Doped Ni(OH)$_2$/Ni Foam	~270	20@ 500 mA/cm^{-2}	1.0 M KOH	25
Fe-NiOH$_x$-25	**210**	**240@ 100 mA/cm^{-2}**	1.0 M KOH	**This work**

Table S2. Impedance parameter values obtained by the fitting of the Nyquist plots in Figure 3e.

Samples	R_s (Ω)	R_{ct} (Ω)
NiOH$_x$	2.105	1.867
Fe-NiOH$_x$-15	1.696	1.160
Fe-NiOH$_x$-25	1.523	0.488
Fe-NiOH$_x$-35	1.647	0.997

References

(1) W. Qiu, Y. Li, A. You, Z. Zhang, G. Li, X. Lu and Y. Tong, *J. Mater. Chem.,* 2017, **5**, 14838-14846.

(2) L. Huang, H. Shin, W. Goddard and J. Wang, *Nano Energy,* 2020, **75**, 104885.

(3) G. Kresse and J. Furthmuller, *Phys. Rev. B,* 1996, **54**, 11169-11186.

(4) V. I. Anisimov, J. Zaanen and O. K. Andersen, *Phys. Rev. B,* 1991, **44**, 943-954.

(5) A. I. Liechtenstein, V. I. Anisimov and J. Zaanen, *Phys. Rev. B,* 1995, **52**, R5467-R5470.

(6) A. J. Tkalych, K. Yu and E. A. Carter, *J. Phys. Chem. C,* 2015, **119**, 24315-24322.

(7) Y. F. Li and A. Selloni, *ACS Catal.,* 2014, **4**, 1148-1153.

(8) J. M. P. Martirez and E. A. Carter, *Chem. Mater.,* 2018, **30**, 5205-5219.

(9) H. Zhong, T. Liu, S. Zhang, D. Li, P. Tang, N. A. Vante and Y. Feng, *J. Energy Chem.,* 2019, **33**, 130-137.

(10) H. Zhong, R. Tian, X. Gong, D. Li, P. Tang, N. A. Vante and Y. Feng, *J. Power Sources,* 2017, **361**, 21-30.

(11) L. Qian, Z. Lu, T. Xu, X. Wu, Y. Tian, Y. Li, Z. Huo, X. Sun and X. Duan, *Adv. Energy Mater.,* 2015, **5**, 1500245.

(12) M. K. Bates, Q. Jia, H. Doan, W. Liang and S. Mukerjee, *ACS Catal.,* 2016, **6**, 155-161.

(13) C. Tang, H. S. Wang, H. F. Wang, Q. Zhang, G. L. Tian, J. Q. Nie and F. Wei, *Adv. Mater.*, 2015, **27**, 4516-4522.

(14) N. Han, F. Zhao and Y. Li, *J. Mater. Chem. A,* 2015, **3**, 16348-16353.

(15) R. Shi, J. Wang, Z. Wang, T. Li and Y. F. Song, *J. Energy Chem.,* 2019, **33**, 74-80.

(16) V. Maruthapandian, M. Mathankumar, V. Saraswathy, B. Subramanian and S. Muralidharan, *ACS Appl. Mater. Inter.,* 2017, **9**, 13132-13141.

(17) J. S. Sun, Y. T. Zhou, R. Q. Yao, H. Shi, Z. Wen, X. Y. Lang and Q. Jiang, *J. Mater. Chem. A,* 2019, **7**, 9690-9697.

(18) G. Liu, X. Gao, K. Wang, D. He and J. Li, *Int. J. Hydro. Energy,* 2016, **41**, 17976-17986.

(19) J. G. Li, H. Sun, L. Lv, Z. Li, X. Ao, C. Xu, Y. Li and C. Wang, *ACS Appl. Mater. Inter.,* 2019, **11**, 8106-8114.

(20) L. Yu, J. F. Yang, B. Y. Guan, Y. Lu and X. W. Lou, *Angew. Chem. Int. Ed.,* 2018, **57**, 172-

176.

(21) A. C. Pebley, E. Decolvenaere, T. M. Pollock and M. J. Gordon, *Nanoscale,* 2017, **9**, 15070-15082.

(22) F. Ksenia, C. Petko, Z. Ivelina, S. Johannes, S. Goran, D. Markus, M. Alexander, P. Aneil, B. Sebastian, S. Christina, B. Thomas and F. R. Dina, *ACS Nano,* 2015, **9**, 5180-5188.

(23) G. Wu, W. Chen, X. Zheng, D. He, Y. Luo, X. Wang, J. Yang, Y. Wu, W. Yan, Z. Zhuang, X. Hong and Y. Li, *Nano Energy,* 2017, **38**, 167-174.

(24) Z. Wu, Z. Zou, J. Huang and F. Gao, *J. Catal.,* 2018, **358**, 243-252.

(25) J. T. Ren, G. G. Yuan, C. C. Weng, L. Chen and Z. Y. Yuan, *Nanoscale,* 2018, **10**, 10620-10628.